16th Australasian Fluid Mechanics Conference
Crown Plaza, Gold Coast, Australia
2-7 December 2007

Analysis of scale energy budgets in wall turbulence using dual plane PIV

N. Saikrishnan [1], E. K. Longmire [1] and I. Marusic[2]

[1]Department of Aerospace Engineering & Mechanics
University of Minnesota, Minneapolis, 55455 USA

[2]Department of Mechanical Engineering
University of Melbourne, Victoria, 3010 AUSTRALIA

Abstract

The scale energy budget in the near wall region is a subject of great interest in turbulent flows since it combines concepts from independent analysis in physical space and scale space. Earlier, this energy budget was studied numerically using Direct Numerical Simulation (DNS) data and experimentally using low resolution dual plane Particle Image Velocimetry (PIV) data. It was observed that the low resolution PIV data were not sufficient to accurately capture the dynamics of the energy balance and hence high resolution experiments were conducted in similar experimental conditions. The results from these high resolution data conducted in two locations of the logarithmic layer of the boundary layer indicate that the resolution of these experiments is sufficient to capture the scale energy budget in the near wall region. Predictions of the cross-over scale, which is related to the relative importance of production and transfer of turbulent kinetic energy, are found to match expected trends, and illustrate that the experimental technique provides a powerful tool for the scale energy budget analysis.

Introduction

Turbulent wall-bounded flows such as boundary layers and channel flows possess a strong anisotropy due to the presence of a strong mean velocity gradient, which can be seen from the production of turbulent kinetic energy in the energy balance equation. This inhomogeneity in the wall-normal direction leads to a spatial redistribution of energy, and hence leads to the classification of the near wall region into generic layers such as the viscous sublayer, the buffer layer, the logarithmic layer and the outer flow. As the name suggests, the viscous sublayer is dominated by viscous effects, whereas the buffer layer is the region where most of the production of turbulent kinetic energy takes place. The logarithmic region is nominally in equilibrium where the production and dissipation balance each other, while the outer region mostly feeds on the energy produced closer to the wall. A clear picture of the dynamics of energy between these regions is crucial to understanding of turbulent boundary layers.

However, this view based on spatial transfer of energy alone is insufficient to completely describe the energy dynamics occurring in the near-wall region and a parallel view based on the decomposition of the flow field into a hierarchy of scales is required to understand observed phenomena. Kolmogorov [6] stated that "in the limit of infinite Reynolds numbers, all the possible symmetries of the Navier-Stokes equation, usually broken by the mechanisms producing turbulence, are restored in a statistical sense at small scales and away from boundaries.", implying the isotropy of turbulent flow at the smallest scales. Also, it was argued that in the logarithmic layer, the longitudinal energy spectrum is proportional to the wavenumber to the power $-5/3$ ($k^{-5/3}$), which was experimentally verified by Saddoughi et al [10]. The turbulent kinetic energy is injected into the system by the direct action of the shear at scales larger than those in the inertial range. Hence, a lot of effort has been devoted towards elucidating the spectral dynamics of turbulent kinetic energy, with an aim to understand the interaction between different scales in the flow.

Given this framework, it is imperative that an integrated approach combining concepts and features from physical space and scale space must be used to describe the energy dynamics in turbulent wall-bounded flows, enabling the study of scale-dependent dynamics in inhomogeneous conditions. The Kármán-Howarth equation represents an evolution equation for the longitudinal autocorrelation function and provides the basis for the Kolmogorov equation for stationary, homogeneous, isotropic turbulence. A generalized version of the Kolmogorov equation for inhomogeneous conditions was derived by Hill [4] and hence provided the framework relating the various processes occurring at different regions of the boundary layer over a wide range of scales. This equation was the basis of an analysis by Marati et al [8], where the equation was appropriately simplified for a Direct Numerical Simulation (DNS) of a turbulent channel flow, and the contributions of different processes in the energy budget in a low Reynolds number flow were calculated. Recently, an identical analysis was presented in Saikrishnan et al [11], where both Dual Plane PIV and DNS data were used to assess the scale energy budget in boundary layer and channel flows. The current work discusses results from high resolution experiments conducted in the inner logarithmic layer of a turbulent boundary layer over a flat plate and compares the trends seen with earlier results in the same experimental facility and DNS data of comparable Reynolds numbers.

Mathematical relations for the scale energy budget

For the present analysis, definitions of relevant variables and expressions are provided below. $u_i(x_i)$ represents the velocity vector at a location x_i. The velocity increment δu_i equals $u_i(x_i+r_i)-u_i(x_i)$. $<\delta u^2>=<\delta u_i \delta u_i>$ represents the amount of fluctuation energy contained at scale $r=\sqrt{r_i r_i}$ and hence is known as the scale energy. Using a change in variables to the scale r_i and the midpoint of the line joining the two points $X_{ci}=\frac{1}{2}(x_i+x_i+r_i)$ gives an equation dependent on these two variables. Kolmogorov [6] provided an equation for the turbulent kinetic energy for homogeneous, isotropic turbulence:

$$\frac{\partial <\delta u^2 \delta u_i>}{\partial r_i} = -4<\varepsilon> + 2\nu \frac{\partial^2 <\delta u^2>}{\partial r_i \partial r_i}. \qquad (1)$$

Here, ε is the one-point pseudo-dissipation given by $\varepsilon = \nu < \partial u_i/\partial x_j \partial u_i/\partial x_j >$. The term on the left hand side represents the energy transfer between scales, while the rightmost term is the viscous diffusion term. This equation is derived from the classical Kármán-Howarth equation [12], which was an evolution equation for the longitudinal autocorrelation function derived from the Navier-Stokes equation.

The logical extension of this analysis is to homogeneous shear

flows, where the production of energy due to the mean shear must also be considered. In the current analysis, the streamwise, wall-normal and spanwise directions are represented by x, y and z, and the corresponding fluctuating velocities are represented by u, v and w. In the modified equation 2, the second term on the left hand side is the inertial contribution from the mean shear, and the third term is the production term due to the mean shear, as discussed in Casciola et al [1].

$$\frac{\partial < \delta u^2 \delta u_i >}{\partial r_i} + \frac{\partial < \delta u^2 \delta U >}{\partial r_x} + 2 < \delta u \delta v > \frac{dU}{dy} = -4 < \varepsilon > + 2\nu \frac{\partial^2 < \delta u^2 >}{\partial r_i \partial r_i}. \quad (2)$$

Hill [4] provided a generalized form of the above equation for inhomogeneous conditions, and for a simple shear with a mean velocity U(y) in the x-direction, it reduces to

$$\frac{\partial < \delta u^2 \delta u_i >}{\partial r_i} + \frac{\partial < \delta u^2 \delta U >}{\partial r_x} + 2 < \delta u \delta v > \left(\frac{dU}{dy}\right)^* + \frac{\partial < v^* \delta u^2 >}{\partial Y_c} = -4 < \varepsilon^* > + 2\nu \frac{\partial^2 < \delta u^2 >}{\partial r_i \partial r_i} - \frac{2}{\rho} \frac{\partial < \delta p \delta v >}{\partial Y_c} + \frac{\nu}{2} \frac{\partial^2 < \delta u^2 >}{\partial Y_c^2}, \quad (3)$$

where Y_c is the wall-normal location of interest and * denotes a mid-point average e.g. $\varepsilon^* = \frac{1}{2}(\varepsilon(x_i) + \varepsilon(x_i + r_i))$. In the above equation, terms with derivatives in r_i represent contributions in scale space, while terms with derivatives in Y_c are in physical space.

The concept of an energy dissipation rate averaged over a sphere in r-space, i.e. $< \varepsilon >_{r_{sphere}}$ was first introduced by Oboukhov [9] in order to mitigate the effect of anisotropy and to account for the strong variability of the energy dissipation rate. This concept, which was also incorporated in Kolmogorov's Refined Similarity Hypothesis (RSH) [7], has been a central concept in the study of small scale turbulence dynamics. However, in the case of both boundary layer and channel flows, the use of three dimensional averaging volumes is not strictly applicable due to the strong inhomogeneity in the wall-normal direction. As a result, averaging is performed on two-dimensional square domains of side r in wall-parallel planes, enabling the study of the role of energy flow across scales at a given wall-normal location.

$$Q_r(r, Y_c) = \frac{1}{r^2} \int_0^r \int_0^r q(r_x, 0, r_z | Y_c) dr_x dr_z, \quad (4)$$

where Q and q represent a generic quantity.

Averaging in wall-parallel planes eliminates the second term on the left hand side in equation 3, as $\delta U = 0$ when $r_y = 0$. The r-averaged equation can now be written in a simple form as

$$T_r + \Pi + T_c = E + D_r + P + D_c, \quad (5)$$

where each term represents the corresponding term in equation 3 and is a function of (r, Y_c). Specifically, T_r gives the inertial contribution to the scale-energy flux in r-space, Π is the production term, T_c is the inertial contribution to the spatial flux of scale-energy and is strictly associated with inhomogeneity, E is the dissipation term, D_r and D_c are the diffusive components of the flux in r-space and in geometric space, respectively, and, finally, P is an inhomogeneous contribution related to the pressure-velocity correlation.

It is seen that the amount of scale energy effectively available at a given wall-normal location Y_c is provided by the local production Π plus all the terms corresponding to a spatial transfer of scale-energy to (or from) the location considered. By grouping the production, the transport in the wall-normal direction and the pressure-velocity term, an effective production is defined as $\Pi_e = \Pi + T_c - P$. Analogously, the contributions of diffusive nature can be added to form an effective dissipation rate, $E_e = E + D_c + D_r$, as the sum of the actual dissipation and the diffusive fluxes of scale-energy in physical and r-space, respectively. With these definitions, equation 5 is expressed in a concise form as

$$T_r(r, Y_c) + \Pi_e(r, Y_c) = E_e(r, Y_c). \quad (6)$$

This expression implies that the transfer across scales plus the effective production must equal the effective dissipation. This relation will hold through the various regions of the boundary layer; however the relative importance of each term varies with the location. This balance has been studied using DNS data from a channel flow at friction Reynolds number $Re_\tau = 180$ by Marati et al [8] and using DNS data from a channel flow at $Re_\tau = 934$ and PIV data in a boundary layer at $Re_\tau = 1160$ by Saikrishnan et al [11]. In this work, a comparison between experimental data of different spatial resolutions and DNS data was made, and it was concluded that increasing the spatial resolution of dual plane PIV data helped to compute the terms of the energy balance more accurately. The present work seeks to extend the analysis in Saikrishnan et al [11] to the inner part of the logarithmic region of the boundary layer.

Description of the experiments

The experimental data presented in this paper were obtained using dual plane particle image velocimetry (PIV). This technique, first presented by Kähler et al [5], has been successfully used to resolve the complete velocity gradient tensor in turbulent boundary layers. The present experiments were conducted in a nominally zero pressure gradient flow over a flat plate in a suction-type boundary layer wind tunnel. The pressure gradient was adjusted in the test section using movable upper walls, which were required to account for the growth of the boundary layer in the streamwise direction. The experiments were conducted in measurement planes located 3.3m downstream of a trip wire, which made the flow fully turbulent in the region of interest. The boundary layer thickness at this location was measured to be 70.8mm. All quantities are normalized using inner variables i.e. the skin-friction velocity U_τ and the coefficient of kinematic viscosity ν, and are denoted using the superscript $+$. It must be noted that all the experiments had an almost identical setup and processing technique except for the resolution, exact field of view and wall-normal locations. The appropriate experimental parameters are listed in Table 1.

The present experimental setup is identical to the one used in Ganapathisubramani et al [3], where the complete velocity gradient tensor was obtained at a given wall-normal location using a three-camera setup, as shown in figure 1. The setup consisted of two independent PIV systems which captured images of olive oil droplets of size $\sim 1\mu$m, generated using eight Laskin nozzles upstream of the flow. The first system was a stereoscopic setup, used to measure all three velocity components within a plane, while the second system was a conventional PIV system that measured the in-plane velocity components in a neighboring plane above it.

The stereoscopic system consisted of two TSI Powerview Plus

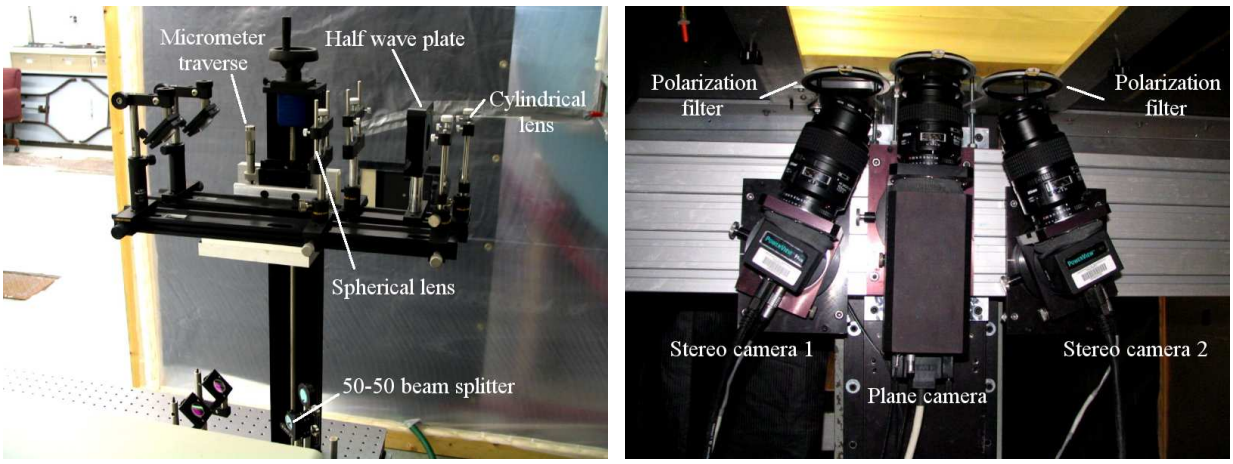

(a) (b)

Figure 1: (a) Photograph of the optical setup to generate the two light sheets. (b) Photograph of the cameras and filters.

	Re_τ	y^+	Δx^+	Δz^+	L_x/δ	L_z/δ
HRPIV1	1130	100	10.0	10.0	0.44	0.44
HRPIV2	1130	47	7.1	7.1	0.31	0.31
DNS1	934	99	11.4	5.7	8π	3π
DNS2	934	47	11.4	5.7	8π	3π

Table 1: Parameters of the experimental and numerical data.

$2k \times 2k$ pixel resolution cameras with Nikon Micro-Nikkor 105 mm lenses while the second system used a Kodak Megaplus $1k \times 1k$ pixel resolution camera with a Nikon Micro-Nikkor 60 mm lens. In order to isolate the two systems from each other, the cameras were fitted with appropriate Polaroid filters. The filters on the stereoscopic system allowed only horizontally polarized light to pass through, whereas the filters on the plane PIV system allowed only vertically polarized light to pass through. The laser sheets were generated by a Spectra-Physics PIV-400-15 Nd:YAG laser system, pulsing about 320 mJ/pulse at 15 Hz. The horizontally polarized beams coming out of the laser were split into two using a CVI Laser $50-50$ non-polarizing beam splitter. Then, one of the beams was passed through a CVI Laser half-wave plate to rotate the polarization by 90°. A combination of spherical and cylindrical lenses were used to form a thin laser sheet from the laser beam. The vertically polarized sheet was seen only by the plane PIV camera, while the horizontally polarized sheet was used for the stereo system. The spacing between the two sheets was adjusted using a micrometer traverse. The thickness of the laser sheets in the region of interest was about 0.4mm, which was controlled by the position of the spherical lens on the traverse shown in figure 1(a). The vertical spacing between the sheets was 0.5mm and 0.4mm for HRPIV1 and HRPIV2 respectively.

The images were acquired using TSI Insight^{TM}3G on two independent workstations in sets of 40 image pairs at a time. This number was determined by the amount of RAM available on the workstations to store the images in temporary memory before downloading onto the hard disk. The sampling rate was set at 1Hz, which was low enough that all image pairs captured independent velocity fields. In order to synchronize the two independent systems and to control the frequency of acquisition of images, a timing system consisting of a master timing box (BNC-500A) and laser timing box (BNC-500C) was used. This system enabled the laser to be pulsed at the design frequency of 15Hz, while sampling at 1Hz. To achieve statistical convergence of ensemble averaged quantities, a very large number of independent velocity fields were acquired and over 1300 images pairs were used for both the experiments. It was verified that this provided very well statistically converged values of averaged quantities. The PIV processing to obtain the vector fields used the adaptive central difference technique of Wereley et al [13], which is briefly described below for the stereoscopic data. In the software, this is referred to as Recursive Nyquist Grid processing. Initially the two images were interrogated using a two-frame cross-correlation on coarse 64×64 pixel windows, with 50% overlap, and the mean displacement calculated. In the next step, this image was again interrogated using a 32×32 pixel window. At this step, the interrogation box in frame 1 was offset upstream and the frame 2 box was offset downstream by half the mean displacement calculated in the previous step. Thus, the final interrogation window size was 32×32 pixels and a 50% overlap was used.

Due to the overlap used during PIV interrogation, the smallest scale resolved is twice the spacing of the vectors. The data from the $1k \times 1k$ cameras were also interrogated using the same method described above. In order to match the resolution between the two systems, the interrogation in this system proceeded from 32×32 pixels down to 16×16 pixels. The vector fields were validated using a standard Gaussian engine that removed vectors with values outside 4 standard deviations from the mean. Any missing vectors were interpolated using a 3×3 local mean technique. The number of spurious vectors was close to 4% in the stereo system and about 2% in the single camera system.

Once the two vector fields from the stereoscopic setup were obtained, they were used in tandem to generate fields for u, v and w on plane 1. The calibration for the stereoscopic setup was performed using the Perspective Calibration software in Insight^{TM}3G. The calibration made use of a single surface target which was traversed in the wall-normal direction on either side of the plane of interest. The software analyzed the calibration target images and found the location of each calibration marker point in the sequence of image frames and matched the image (X,Y) location to the target marker (x,y,z) location in the fluid. This set of calibration points was used to create a calibration mapping function, which was used to generate the

velocity fields in plane 1. The data from the two planes were used to compute the entire velocity gradient tensor in the lower plane. For the in-plane gradients, a second-order central difference scheme was used, while a first-order forward differencing scheme was used to calculate the streamwise and spanwise velocity gradients in the wall-normal direction. Finally, the wall-normal gradient of the wall-normal velocity was recovered from the continuity equation. Thus the complete velocity gradient tensor was obtained. The uncertainties in each quantity are discussed in detail in Ganapathisubramani et al [3].

The DNS dataset under consideration here is a numerical simulation of a fully developed channel flow. The numerical technique involved the integration of the Navier-Stokes equations in the form of evolution problems for the wall-normal vorticity and the Laplacian of the wall-normal velocity. For spatial discretization, Chebychev polynomials were used in the wall-normal direction, while de-aliased Fourier expansions were utilized in wall-parallel planes. The temporal discretization used is a third-order semi-implicit Runge-Kutta scheme. Further details of the DNS can be found in del Álamo et al [2]. The simulation of interest, referred to as *L*950 in the paper, has an $Re_\tau = 934$. This DNS dataset was used to assess the scale energy budget numerically. It must be observed that the numerical data are obtained in a channel flow, while the experimental data are obtained in a zero pressure gradient flow over a flat plate, which are fundamentally different flows in spite of the similar Re_τ. However, it is expected that for $y/\delta \leq 0.6$, the effect of the opposing wall in the channel flow should be minimal. It must be noted from table 1 that the size of the DNS data field was extremely large in comparison to the PIV data, and for the current analysis, data from two independent timesteps were used, and it was verified that these provided well converged ensemble averaged values.

Results and Discussion

The results of the scale-by-scale analysis are presented in the following section. For all figures, the solid line represents the effective production Π_e, the dash-dotted line represents the scale transfer term T_r, the dashed line represents E_e and the symbols show the sum $(\Pi_e + T_r)$. Figures 2 and 3 illustrate the scale by scale energy budget for the experimental dual plane PIV data from HRPIV1 and HRPIV2 respectively. The main observation from these two plots is that magnitude of the terms of the energy budget is higher at $y^+ = 47$ than at $y^+ = 100$. For example, the maximum value for the production term at $y^+ = 47$ is 0.38, while at $y^+ = 100$, the maximum value is only about 0.10. This seems to be in accordance with what is expected in a boundary layer, that energy dynamics are stronger closer to the wall in the logarithmic region. The second observation is that at $y^+ = 100$, the curves for the production and transfer cross-over at a scale which is referred to as the cross-over scale (l_c^+). At scales smaller than cross-over scale, the scale energy transfer is the larger term, whereas at larger scales, the production takes over as the dominant mechanism. This difference in the balance of energy between the various terms could prove invaluable for numerical modeling and assumptions therein. The interpretation and significance of the cross-over scale was discussed in detail by Marati et al [8]. At $y^+ = 100$, the cross-over scale is seen to occur at $l_c^+ = 63$. In contrast, the corresponding curves at $y^+ = 47$ seen in figure 3 do not cross-over each other at all, i.e. the production is always larger than the transfer term, implying the absence of a cross-over scale. It was observed in [8] that at $Re_\tau = 180$, a cross-over between the production and transfer first occurs at around $y^+ = 20$, and the cross-over scale increases with distance from the wall.

Figures 4 and 5 show the scale by scale energy balance obtained

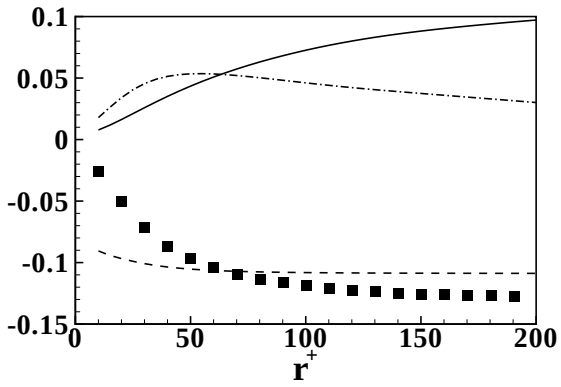

Figure 2: Detailed energy balance for HRPIV1 ($y^+ = 100$). The solid line is $-\Pi_e$, the dash-dotted line is $-T_r$, the dashed line is E_e and the symbols represent the sum $(\Pi_e + T_r)$. All terms are normalized with wall variables ν and U_τ.

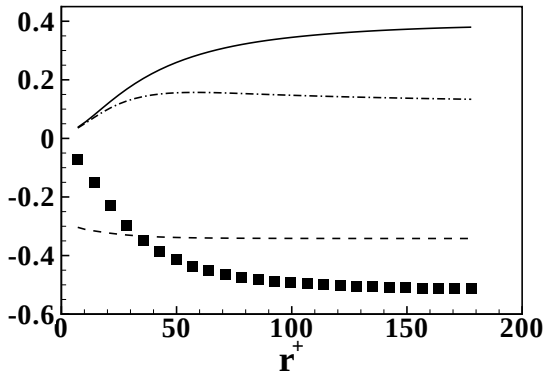

Figure 3: Detailed energy balance for HRPIV2 ($y^+ = 47$). Legend is same as in Figure 2.

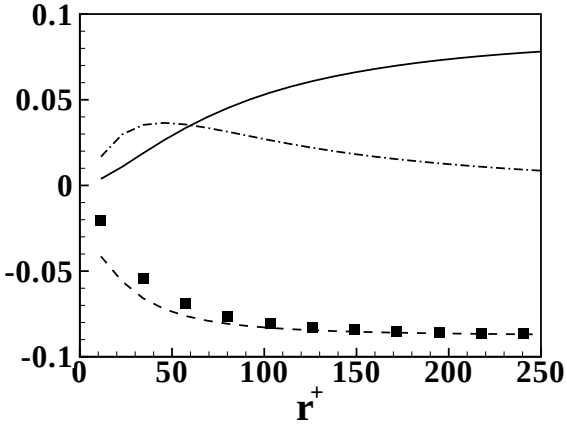

Figure 4: Detailed energy balance for DNS1 ($y^+ = 99$). Legend is same as in Figure 2.

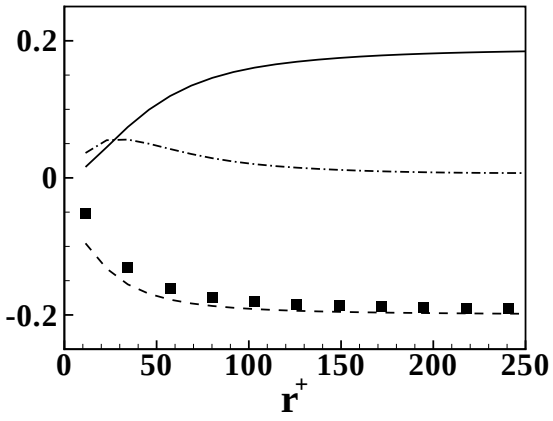

Figure 5: Detailed energy balance for DNS2 ($y^+ = 47$). Legend is same as in Figure 2.

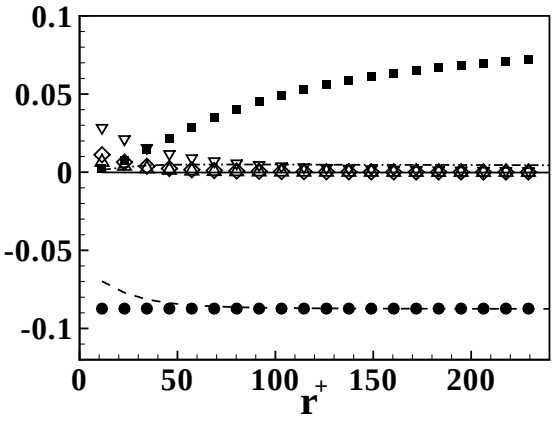

Figure 6: Individual contributions to terms for HRPIV1 ($y^+ = 99$). The filled squares represent the production Π, the filled circles represent the dissipation E, the solid line is the diffusion in physical space D_c, the dash-dotted line is the transfer in physical space T_c, the open symbols represent the three terms of the diffusion in scale space i.e. $\triangle$ - D_{rx}, ∇ - D_{ry}, $\diamondsuit$ - D_{rz} and the dashed line is $(E_e - D_{ry})$.

from the DNS data at $Re_\tau = 934$ in the logarithmic layer. Comparing these plots to the results from the experimental data, we see that the same qualitative trends are observed in the curves for the production and transfer terms. Similarly, it is seen that the magnitude of these terms is larger closer to the wall. The other main observation from these plots is the close match between the sum of the production and transfer terms and the dissipation term, shown in the lower part of the figures. This indicates that the calculated values match equation 6, and hence provide a very good estimate of the cross-over scale. In contrast, it is seen that the balance is not as accurate in the experimental data. However, it must be noted that in figure 2, the balance is almost accurate at larger scales, whereas it is less accurate in figure 3. This mismatch can be analyzed in two separate regimes - small scales and large scales.

Figure 6 shows the contributions of the individual terms in equation 5 for the DNS data at $y^+ = 99$. This shows that in the effective production, the production term is the dominant term, while in the effective dissipation term, the dissipation is the largest contributor. However, the diffusion terms represented by the open symbols in the figure have a significant contribution at small scales. It must be noted that in the experimental data, it is not possible to calculate the D_{ry} term since only two planes of data are available and this term is mostly made up of second derivatives in the wall-normal direction. As can be seen in the figure, the term D_{ry} represented by the ∇ symbol has a significant contribution at small scales. The dashed line shows the effective dissipation term without the contribution of D_{ry}, which looks identical to the effective dissipation curves from the experimental data. This explains the mismatch in the curves at small scales from the PIV data.

The mismatch at the larger scales appears to be a limitation of the resolution of the experiment and as stated earlier, the mismatch is greater closer to the wall. This might be explained as follows. Closer to the wall, the smallest scale in the flow, i.e. the Kolmogorov scale, becomes smaller, since it is inversely proportional to the square root of the dissipation, which is higher closer to the wall in the logarithmic layer. This implies that better resolution is needed to accurately compute the velocity gradients and hence the dissipation. It must be noted is that the in-plane resolution, which affects the x and z gradients, are expected to be more accurate in the PIV data since the resolution here is much better than the numerical data (table 1). Hence, it is expected that the reason for the mismatch at the larger scales is mostly due to errors in the wall-normal gradients calculated experimentally. In the DNS data, the wall-normal gradients are calculated using data from 3 planes spaced around the location of interest with a spacing smaller than achievable in the experiment. The gradients in velocity are higher closer to the wall, which implies that for the same spacing between planes in the wall-normal direction, the first order finite differencing could result in higher errors closer to the wall. On the other hand, in the DNS data, due to the use of Chebychev polynomials in the wall-normal direction, the grid is more finely spaced closer to the wall, which yields more accurate wall-normal derivatives. For example, at $y^+ = 110$, the average wall-normal spacing of planes was about 3.6 wall units, as compared to a spacing of around 8 wall units in the PIV data. At $y^+ = 47$, the wall-normal spacing in the DNS data was 2.4 wall units. Thus, a more accurate calculation of the wall-normal gradients is expected in the DNS data and this explains the mismatch in the curves at large scales in the PIV data.

The estimate of the cross-over scale l_c^+ for the DNS data at $y^+ = 100$ is about 60, while it is about 63 for the PIV data, which implies a reasonable agreement between the experiment and numerical simulation. In the analysis by [8], it was argued that the cross-over scale must vary linearly with the product of the Karman constant and the wall-normal location. The values of l_c^+ obtained from both the DNS and the PIV data in the current analysis are found to be higher than the earlier predictions, seeming to indicate a Reynolds number effect on the cross-over scale. This point needs to be studied further by conducting the scale budget analysis using experimental and numerical data at other locations of the boundary layer. Figure 5 indicates a cross-over scale of about 27 at $y^+ = 47$, but the PIV data at the same location does not seem to yield a cross-over scale, since the production is always greater than the transfer term. This is one of the main differences between the two datasets at $y^+ = 47$. The final observation is that the magnitudes of the terms are much higher in the PIV data as compared to the DNS data. At this point, there does not seem to be a logical explanation to this feature and will form a major part of future work to be undertaken.

Conclusions and Future Work

The scale by scale energy budget was derived and calculated for dual plane PIV in a turbulent boundary layer and DNS data from a fully developed channel flow at two locations in the logarithmic region of the boundary layer. It was seen that the numerical data yielded a much better agreement to the energy budget equation, which is possibly caused by the better accuracy in wall-normal gradients. It was demonstrated that at $y^+ = 100$, the dual plane PIV method provided a reliable experimental tool to study the scale energy dynamics, while closer to the wall, a deviation from the numerical data was observed. The overall trends of the various terms of the budget seemed to agree well between the numerical and experimental data, suggesting that dual plane PIV has the potential to be the appropriate experimental tool to study the scale by scale energy budget.

The major challenge ahead is to be able to tune the experimental setup to obtain a better balance between the terms, similar to the DNS data. In this regard, further experiments must be conducted with varying experimental parameters, in order to arrive at the optimal parameters necessary to accurately obtain estimates of the terms of the energy budget. Specifically, the focus will be on analyzing the effect of the sheet spacing in the wall-normal direction in the experiment on the terms of the energy budget. It is also expected that studies on spatial resolution and sheet thickness would yield further insights into improving the experimental setup. Further analysis is also required to resolve the issue of the higher magnitude of values from the PIV data as compared to the DNS data. Once it has been adequately demonstrated that the technique is suitable for analysis at various wall-normal locations, it is possible to extend the current analysis to higher Reynolds numbers, which can be obtained experimentally in the current facility. The additional data will also provide us with an insight into the Reynolds number dependencies of the current analysis.

Acknowledgements

The authors would like to acknowledge the effort of Dr. Elisabetta De Angelis, Dr. Carlo Casciola, Dr. Renzo Piva and Dr. Nicoletta Marati for the development of the scale by scale energy budget analysis and useful discussions. The authors gratefully acknowledge support from the National Science Foundation through Grant CTS-0324898, the David and Lucile Packard Foundation and the Australian Research Council.

References

[1] Casciola, C. M., Gualtieri, P., Benzi, R. and Piva, R., Scale-by-scale budget and similarity laws for shear turbulence, *J. Fluid Mech.*, **476**, 2003, 105–114.

[2] del Álamo, J. C., Jiménez, J., Zandonade, P. and Moser, R. D., Scaling of the energy spectra of turbulent channels, *J. Fluid Mech.*, **500**, 2004, 135–144.

[3] Ganapathisubramani, B., Longmire, E. K., Marusic, I. and Pothos, S., Dual-plane PIV technique to determine the complete velocity gradient tensor in a turbulent boundary layer, *Exp. Fluids*, **39**, 2005, 222–231.

[4] Hill, R. J., Exact second-order structure-function relationships, *J. Fluid Mech.*, **468**, 2002, 317–326.

[5] Kähler, C. J. and Kompenhans, J., Fundamentals of multiple plane stereo particle image velocimetry, *Exp. Fluids*, **29**, 2000, 70–77.

[6] Kolmogorov, A. N., The local structure of turbulence in incompressible viscous fluid for very large reynolds numbers, *Dokl. Akad. Nauk SSSR*, **30**, 1941, 9–13.

[7] Kolmogorov, A. N., A refinement of previous hypotheses concerning the local structure of turbulence in a viscous incompressible fluid at high reynolds number, *J. Fluid Mech.*, **13**, 1962, 82–85.

[8] Marati, N., Casciola, C. M. and Piva, R., Energy cascade and spatial fluxes in wall turbulence, *J. Fluid Mech.*, **521**, 2004, 191–215.

[9] Oboukhov, A. M., Some specific features of atmospheric turbulence, *J. Fluid Mech.*, **13**, 1962, 77–81.

[10] Saddoughi, S. G. and Veeravalli, S. V., Local isotropy in turbulent boundary layers at high Reynolds number, *J. Fluid Mech.*, **268**, 1994, 333–372.

[11] Saikrishnan, N., Longmire, E. K., Marusic, I., Marati, N., Casciola, C. M. and Piva, R., Use of dual plane PIV to assess scale-by-scale energy budgets in wall turbulence, in *Advances in Turbulence XI : Proceedings of the 11th EUROMECH European Turbulence Conference*, editors J. M. L. M. Palma and A. Silva Lopes, 2007, 343–345, 343–345.

[12] von Kármán, T. and Howarth, L., On the Statistical Theory of Isotropic Turbulence, *Royal Society of London Proceedings Series A*, **164**, 1938, 192–215.

[13] Wereley, S. T. and Meinhart, C. D., Second-order accurate particle image velocimetry, *Exp. Fluids.*, **31**, 2001, 258–268.